Journal of Sol-Gel Science and Technology
https://doi.org/10.1007/s10971-022-05797-x

ORIGINAL PAPER: SOL-GEL AND HYBRID MATERIALS FOR CATALYTIC, PHOTOELECTROCHEMICAL AND SENSOR APPLICATIONS

Preparation and activity evaluation of B_4C/ZnO composite photocatalyst

Ozcan Koysuren[1] · Hafize Nagehan Koysuren[2]

Received: 22 January 2022 / Accepted: 31 March 2022

Abstract

In this study, B_4C/ZnO composite photocatalysts were obtained by the heat treatment of polyvinyl borate composite, synthesized using the crosslinking reaction of polyvinyl alcohol and boric acid in the presence of ZnO nanoparticles. The photocatalytic activity of B_4C/ZnO was evaluated by photocatalytic degradation of a model dye, methylene blue. The relationship between the photocatalytic degradation of methylene blue and the temperature of the reaction medium, and the pH of the reaction medium was also studied. The structural and optical properties of B_4C/ZnO photocatalyst were characterized by Fourier transform infrared (FTIR) spectroscopy, X-ray powder diffraction (XRD) analysis, fluorescence spectroscopy, scanning electron microscopy (SEM), and UV–Vis absorption spectroscopy. The B_4C and B_4C/ZnO composite nanoparticles were synthesized successfully, which was proven by the FTIR, XRD, and SEM analyses. The photocatalytic degradation experiments illustrated that the photocatalytic activity of the composite photocatalysts was higher than that of B_4C on the photocatalytic degradation of the model dye. The heterojunction structure formed between ZnO and B_4C might have decreased the recombination rate, which was determined by the fluorescence spectroscopy. The B_4C/ZnO composites possessed wider optical bandgap compared to pure B_4C, which was determined by Tauc's plot analysis. When compared with pure B_4C, approximately three times faster degradation rate was obtained by the B_4C/ZnO composite. After four cycles of the photocatalytic degradation experiments, approximately 26% loss in the photocatalytic degradation efficiency was observed. Based on the scavenger experiments to reveal the photocatalytic degradation mechanism, the photoinduced holes, the superoxide radicals, and the hydroxyl radicals were the main active species for the degradation of methylene blue.

Supplementary information The online version contains supplementary material available at https://doi.org/10.1007/s10971-022-05797-x.

✉ Ozcan Koysuren
koysuren@ankara.edu.tr

[1] Department of Energy Engineering, Ankara University, Ankara 06830, Turkey

[2] Department of Environmental Engineering, Kirsehir Ahi Evran University, Kirsehir 40100, Turkey

Published online: 23 April 2022

Graphical abstract

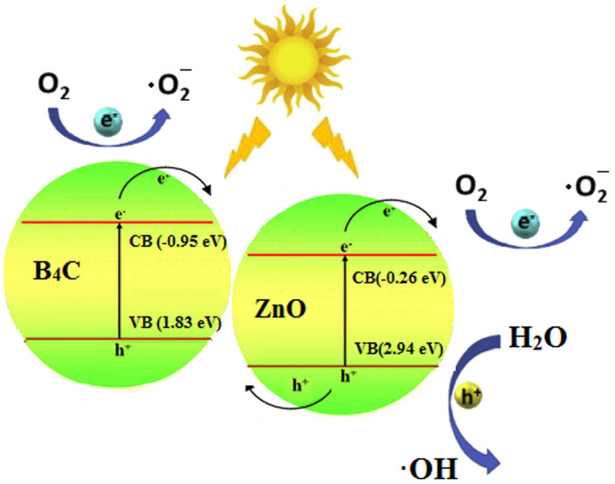

The proposed degradation mechanism of the B_4C/ZnO heterojunction structure

Keywords B_4C · ZnO · Photocatalyst · Heterojunction · Photocatalytic activity

Highlights

- Combining ZnO with B_4C narrowed the optical band gap energy, exhibiting a red shift.
- The recombination rate of ZnO and B_4C was reduced.
- ZnO enhanced the photocatalytic degradation efficiency of B_4C.
- A threefold increase in the reaction rate of the photocatalytic degradation was obtained with the composite.
- Both the hydroxyl and superoxide radicals contributed significantly to the photocatalytic degradation reaction.

1 Introduction

Boron carbide (B_4C) is an important nonoxide ceramic with low density, high modulus, wear resistance, impact resistance, high thermal stability, high neutron absorption, and high hardness properties [1, 2]. B_4C also has high melting temperature, low thermal expansion coefficient, and high chemical resistance. The specified features have made B_4C suitable for wide application in military, electronic and nuclear industries as neutron-absorbing materials, electrode materials, wear-resistant materials, and cutting tools [3, 4]. When compared with micro-scale materials, sub-micron scale or nano-sized materials exhibit different properties. Similarly, nano-size B_4C has superior properties and more homogeneous crystal structure compared to micro-size B_4C. Researchers have been trying to reduce the size of the bulk B_4C to obtain enhanced features. The B_4C nanoparticles have the potential to replace the conventional materials used for tools, molds and wearing parts. The B_4C nanoparticles have been studied as an agent in the cancer treatment. They are utilized as biosensors [5]. In addition, the B_4C nanoparticles have been utilized as reinforcement for ceramic and metal-based composites to improve the wear resistance of the matrix materials [4].

Various techniques such as ball milling of bulk B_4C [2], magnesiothermal reduction of B_2O_3 in the presence of carbon [6], chemical vapor deposition of B_2O_3-activated carbon suspension on the Co-B catalyst nanoparticles [7], carbothermal reduction of B_2O_3 [8], laser fragmentation of large B_4C particles dispersed in ethyl acetate [9], mechanochemical processing of boron oxide with magnesium in the presence of carbon [4], carbothermal reduction of boric acid [5], high-temperature heating of amorphous boron and carbon [10] have been used to prepare the B_4C nanoparticles. However, the mass production of the B_4C nanoparticles has been limited by its complex synthesis techniques. Also, toxic precursors and chemicals are required to prepare the B_4C nanoparticles [1, 2]. Most of these reactions are highly endothermic, requiring high temperature to increase the reaction rate, and time consuming and expensive. Also, the B_4C nanoparticles produced using these techniques are mostly coarse grained. Hence, they need to be ground following their reaction [4]. When examined in detail, the magnesiothermal reduction of B_2O_3 is insufficient to produce high-purity B_4C powders due to magnesium contamination. The carbothermal reduction of B_2O_3 or H_3BO_3 in the presence of a carbon

source at a high temperature ($T > 1750$ °C) results in a product with significant residues of free carbon. The B_4C nanoparticles can be synthesized directly through high-temperature heating of amorphous boron and carbon. However, the specified technique requires high-temperature heating above 1500 °C, long reaction time, and expensive raw materials, making this technique economically unsuitable. Although the chemical vapor deposition technique can produce high purity B_4C nanoparticles, the high costs of gaseous reactants and process equipments render this technique unfavorable for the commercial-scale B_4C nanoparticle production [11]. Due to the problems of currently applied methods such as low yield and expensive material or processing cost, different techniques have been studied to produce the B_4C nanoparticles on a large scale [10].

Researchers have been studying on the use of a single-source solid precursor to obtain B_4C nanoparticles through a simple and straightforward technique [12]. Synthesis of B_4C using a polymer–precursor is an alternative technique to obtain the nanoparticles with a low-temperature process. The polymer-precursor technique provides high reproducibility compared to conventional B_4C production methods [13]. In addition, the final properties of B_4C synthesized using the polymer-precursor technique can be modified by changing the precursor's composition and the process parameters [14]. In this context, different polymer-precursors have been used for synthesizing B_4C nanoparticles such as poly(resorcinol borate) [11], poly(6-norbornenyldecaborane-co-decaborane) copolymer [12], polyvinylpyrrolidone-boric acid [13], boric acid-sucrose [3], xerogel [15] and polyvinyl alcohol-boric acid [16–19] have been utilized to synthesize the polymer-precursor. The synthesis of B_4C through the pyrolysis of a polymer-precursor in an inert atmosphere overcomes the problem of the free carbon residue in the final product. This technique also provides to prepare the B_4C nanoparticles through a low-temperature synthesis path. In this technique, the synthesis of the polymer-precursor is important and mostly hydrothermal reactions are conducted to synthesize the polymer-precursor. Afterward, the polymer-precursor is pyrolyzed in an inert medium to obtain the B_4C nanoparticles [17].

It is not easy to find a low-cost, stable, and efficient photocatalyst, active under natural sunlight or visible light. B_4C as a metal-free semiconducting material is a promising new class of photocatalyst that has not been studied much. This material's attractive electronic structure, chemical and physical stability, and low cost render it potentially useful in a variety of applications as a photocatalyst [19]. According to the density functional theory calculations conducted in the literature, there are crystal defects and distortions in the crystal structure of B_4C, which gives rise to a decrease in its optical bandgap energy. It means that B_4C as a photocatalyst can benefit more from the natural sunlight and the visible light. Meanwhile, the more intense crystal defects and distortions lead to a large number of midgap energy states between the valence band and the conduction band of B_4C, which can reduce the photocatalytic activity by promoting the recombination of the photogenerated electron–hole pairs [20]. When compared with the conventional semiconductors, B_4C, p-type semiconductor, exhibits a longer lifetime (~1 ms) of the photogenerated charge carriers due to its unique structure of the icosahedron unit. Considering the features mentioned, B_4C can be a potential photocatalyst material induced by the natural sunlight or the visible light. There are only a few studies on the photocatalytic activity of B_4C in the literature. B_4C nanoparticles can provide sufficient photocatalytic efficiency only when doped with a metal atom such as Fe, Co, Ni, Cu, and Zn [21], or combined with another semiconductor such as C_3N_4 [22], TiO_2 [23], $Bi_7O_9I_3$ [24] and BiOI [25]. Combining B_4C with a semiconductor photocatalyst in the composite heterojunction structure can reduce the recombination rate of the photoexcited charge carriers, which leads to an improvement in the photocatalytic efficiency [26]. Owing to the heterojunction structure formed between B_4C and another semiconductor, the separation of the photogenerated electron-hole pairs could be achieved and the number of active species, charges, and/or radicals, required for the photocatalytic activity could be increased [23, 25].

ZnO has been preferred as a photocatalyst due to its high optical and photocatalytic activity, natural abundance, non-toxic feature, and low cost [26, 27]. Owing to its wide optical band gap (~3.2 eV), ZnO can be excited only by UV light ($\lambda < 387$ nm). Hence, its photocatalytic activity is limited to the UV light irradiation [27]. In addition, the recombination rate of the photoexcited charge carriers is also high, resulting in low photocatalytic efficiency. The specified negative features affect the practical application of pure ZnO in wastewater treatment [26]. To solve the specified problems, the formation of an internal electric field within the photocatalyst through a heterojunction structure has been proven as an effective method to promote the separation of the photogenerated charge carriers. Considering the energy band structure, combining ZnO with another semiconductor is expected to suppress the recombination of the photoinduced charge carriers on the semiconductors. In order to form a heterojunction structure with ZnO, it is required to select a suitable p-type semiconductor. Within the scope of this study, the B_4C nanoparticles were obtained by the heat treatment of a polymer precursor, synthesized using the crosslinking reaction of polyvinyl alcohol and boric acid. ZnO, n-type semiconductor, was coupled with the p-type semiconductor, B_4C, to form composites with the heterojunction structure. The photocatalytic activity of the as-prepared samples was evaluated by monitoring the photocatalytic degradation of methylene blue under UVA light. Combining B_4C with ZnO has been found

to be an effective method to improve the photocatalytic activity of B_4C. No studies on the photocatalytic activity of B_4C/ZnO have been reported in the literature.

2 Experimental

2.1 Materials and methods

In order to obtain B_4C and the B_4C/ZnO heterojunction structure, polyvinyl borate (PVB), precursor polymer, was synthesized. Polyvinyl alcohol (PVA) (molecular weight 89000–98000 g/mol and 99 mol% hydrolyzed) and boric acid (H_3BO_3), obtained from Sigma-Aldrich, were used to synthesize PVB. All these chemicals were used as received. The precursor polymer (PVB), which contains B-O-C functional groups along its chain structure, was synthesized using the condensation reaction of PVA and boric acid in a PVA-OH:H_3BO_3 molar ratio of 4.2:1. In detail, a certain amount of PVA (2.47 g) was dissolved in distilled hot water (50 ml) at 80 °C. Meanwhile, 0.795 g of boric acid was added into a separate beaker, including distilled water (50 ml). After dissolving PVA and boric acid separately, boric acid solution was added to the PVA solution under stirring. It was kept under stirring for 30 min., resulting in a white slime. Then, the white slime was collected on a petridish and dried at 120 °C. After drying, it was ground to powder. The precursor polymer (PVB) was converted to B_4C nanoparticles by a heat treatment under Ar flow for 3 h. The white slime powders were placed in a ceramic crucible and heated in a tube furnace (Protherm, PTF Series) with a heating rate of 10°/min under Ar flow until it reached the desired temperature. The heat treatment of the precursor polymer at 600 °C for 3 h yielded a black powder in the foam form. The resulting black foam was allowed to cool naturally under Ar flow. After cooling, the black foam was ground to powder [18, 28].

In B_4C/ZnO synthesis, the method followed for pure B_4C synthesis was applied. In a typical experiment, PVA (2.47 g) was dissolved in distilled hot water (50 ml) at 80 °C. ZnO nanoparticles, obtained from Sigma-Aldrich, were added into the PVA solution. As-prepared suspension was kept under stirring for 60 min. The suspensions, meeting the previously adjusted mole ratio of B/ZnO with 1/0, 1/0.25, 1/0.5, 1/1, and 0/1, respectively, were prepared. On other hand, boric acid (0.795 g) was dissolved in distilled water (50 ml). Then, it was added to the suspension. It was kept under stirring for 30 min, which gave rise to the formation of the PVB/ZnO composite in the white slime form. Then, the white slime was collected and dried at 120 °C. After grounding, it was heated in the tube furnace under Ar flow at 600 °C for 3 h. The heat treatment of the PVB/ZnO composite yielded B_4C/ZnO heterojunction nanostructures in the black powder form [18, 28]. In order to distinguish among the samples, they were labeled as B_4C (x%)/ZnO ($x = 100, 80, 67, 50, 0$), respectively.

2.2 Structural, morphological, and optical characterization

Fourier transform infrared (FTIR) spectroscopy of the as-prepared samples, B_4C(100%)/ZnO, B_4C(80%)/ZnO, B_4C (50%)/ZnO, and B_4C(0%)/ZnO, was carried out using Nicolet 6700 (Thermo Scientific) model spectrophotometer in the range of 400–4000 cm^{-1}. FTIR spectra were used to characterize the chemical bonds of both B_4C and ZnO. X-ray diffraction (XRD) patterns of the samples were monitored with a Riguku Ultima IV model X-ray diffractometer by using a CuKα source at a scan rate of 1°/min. The crystal structure of B_4C in the presence and in the absence of ZnO nanocrystals was investigated. The morphology of the samples was studied using a QUANTA 400 F model field emission scanning electron microscope. For the fluorescence spectroscopy analysis, the sample powders were dispersed in distilled water using an ultrasonic bath. The fluorescence spectrum of the samples was measured using a Lumina model fluorescence spectrophotometer (Thermo Scientific). The spectrum data were collected at an excitation wavelength of 325 nm and monitored in the wavelength range of 350 nm to 600 nm.

2.3 Characterization of the photocatalytic performance

Photocatalytic activity of B_4C/ZnO composites was evaluated by photocatalytic degradation of a model dye, methylene blue, in an aqueous solution. A 12 W UVA lamp (310–400 nm) was used for the photocatalytic degradation test. Prior to the UV light irradiation, 0.3 g of the photocatalyst sample was added to a beaker, including 60 ml of methylene blue solution (10 mg/l). The dye solution was at its natural pH (about 6.7). Then, the suspension was stirred in the dark for 30 min. to attain the adsorption-desorption equilibrium. The suspension was irradiated by using the UVA lamp under magnetic stirring. The distance between the UV light and the surface of the suspension was set to 5 cm. After every 20 min. of the UV light irradiation, a sample (2 ml) was taken from the suspension. Then, the sample was centrifuged at 7000 rpm for 1 min. to separate the photocatalyst particles and the clarified dye solution was analyzed using the UV–Vis spectrophotometer (Genesys 10S, Thermo Scientific). The absorbance of the model dye at 664 nm was utilized to calculate the photocatalytic degradation efficiency by using the following Eq. (1) [29]:

$$\text{Photocatalytic degradation efficiency}(\%) = (A_0 - A)/A_0 \quad (1)$$

at which A_0 is the absorbance of the dye solution before the UV light irradiation and A is the absorbance of the dye solution after the UV light irradiation. For the recycle test, the B_4C(50%)/ZnO composite nanoparticles were isolated from the degraded dye solution using centrifugation and they were re-dispersed in a new dye solution after drying. Four subsequent degradation cycles were performed. In addition, to reveal the degradation mechanism of the photocatalyst samples, ammonium oxalate (1 mM) as a hole scavenger (h^+), potassium persulfate (1 mM) as an electron (e^-) scavenger, tert-butanol (1 mM) as hydroxyl (•OH) radical scavenger and ascorbic acid (1 mM) as an superoxide ($•O_2^-$) radical scavenger were added into the dye solution of the B_4C(50%)/ZnO composite, separately. As a process parameter, the effect of the ambient temperature and the ambient pH was also studied with the B_4C(50%)/ZnO composite. The reaction temperature was increased to 42 °C and 62 °C, respectively. In addition, pH of the dye solution was adjusted to 3 and 10 using HCl and NaOH, respectively.

3 Results and discussion

3.1 FTIR analysis

The FTIR spectrum of the as-prepared samples, B_4C (100%)/ZnO, B_4C(80%)/ZnO, B_4C(50%)/ZnO, and B_4C (0%)/ZnO, are shown in Fig. 1. According to the FTIR spectrum of pure ZnO (Fig. 1a), transmittance peaks observed at ~400 cm^{-1}, 487 cm^{-1}, and 522 cm^{-1} were assigned to the Zn-O stretching vibration. The transmittance peak at 880 cm^{-1} was assigned to the symmetric bending of the H-O-H bond. The broadband at around 3420 cm^{-1} and the sharp peak at 2984 cm^{-1} were attributed to the O-H vibration of surface adsorbed water molecules [30]. B_4C was obtained by the heat treatment of the polymer-precursor, PVB, synthesized using polyvinyl alcohol (PVA) and boric acid (H_3BO_3). According to the literature, the hydroxyl group of PVA can react easily with H_3BO_3 through the condensation reaction to form B–O–C bond of the polymer-precursor. During the heat treatment process, first B_2O_3 and carbon phases were formed and then the B_4C crystals were formed through the carbothermal reduction reaction of the B_2O_3 phase with the carbon phase [16]. According to the FTIR spectrum of pure B_4C (Fig. 1b), the peaks observed at 1386 cm^{-1} and 1249 cm^{-1}, which are the characteristic transmittance peaks of the B–O and B-C bonds, respectively, seemed to overlap [31]. In addition, the peak at 1186 cm^{-1} was attributed to the B-C stretching vibration [19]. The transmittance peaks belonging to the B-C bond proved the formation of the B_4C structures. These values agreed with the previous studies from the literature [19, 31]. The presence of the peak belonging to the B-O bond demonstrated that a part of the B_2O_3 phase could not be converted to the B_4C structure during the carbothermal reduction reaction due to the relatively low heat treatment temperature. According to Fig. 1c, d, the characteristic peak of B-C appeared at 1249 cm^{-1} shifted to 1214 cm^{-1} and 1218 cm^{-1} for B_4C(80%)/ZnO and B_4C(50%)/ZnO, respectively. Moreover, the peak intensity of the B-C bond increased and sharpened compared to the corresponding peak of pure B_4C. It means that almost all of the B_2O_3 structure was converted to the B_4C structure in the presence of the ZnO nanoparticles. ZnO could act as a catalyst to enhance the rate of the carbothermal reduction reaction. Also, ZnO could act as a crystal seed to improve the crystallinity of the B_4C structure.

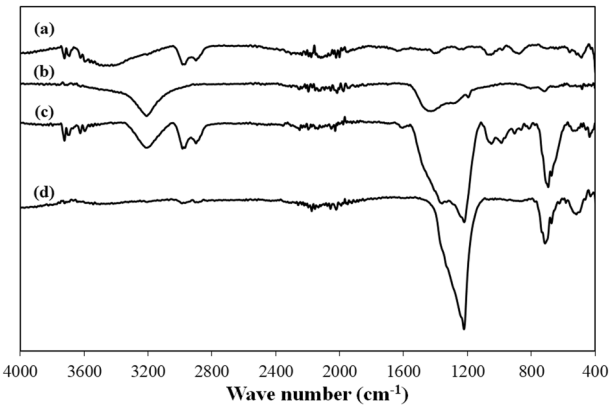

Fig. 1 FTIR spectrum of **a** pure ZnO, **b** pure B_4C, **c** the B_4C(80%)/ZnO composite, and **d** the B_4C(50%)/ZnO composite

3.2 Morphology analysis

Sphere-like structures of different sizes, varying from 100 nm to 1 μm, were observed on the SEM image of B_4C (Fig. 2a). The SEM images also revealed that the crystal structure of B_4C was formed to a certain extent. According to the SEM images of the B_4C(80%)/ZnO, B_4C(67%)/ZnO, and B_4C(50%)/ZnO composites (Fig. 2b–d), the crystallinity of B_4C seemed to be enhanced in the presence of the ZnO nanoparticles. In parallel with the increase in the ZnO content of the composite, the crystallinity of B_4C appeared to be increased. Similar results were found in the XRD pattern of the composite samples. It means that ZnO could act as a seed crystal to enhance the crystallinity of B_4C during its carbothermal reduction reaction. The SEM images of the composite samples also revealed that there was a good interaction between the composite constituents, which was essential in terms of the stable heterojunction structure and the reduction in the recombination rate of the photo-induced charge carriers. It is not easy to distinguish the ZnO

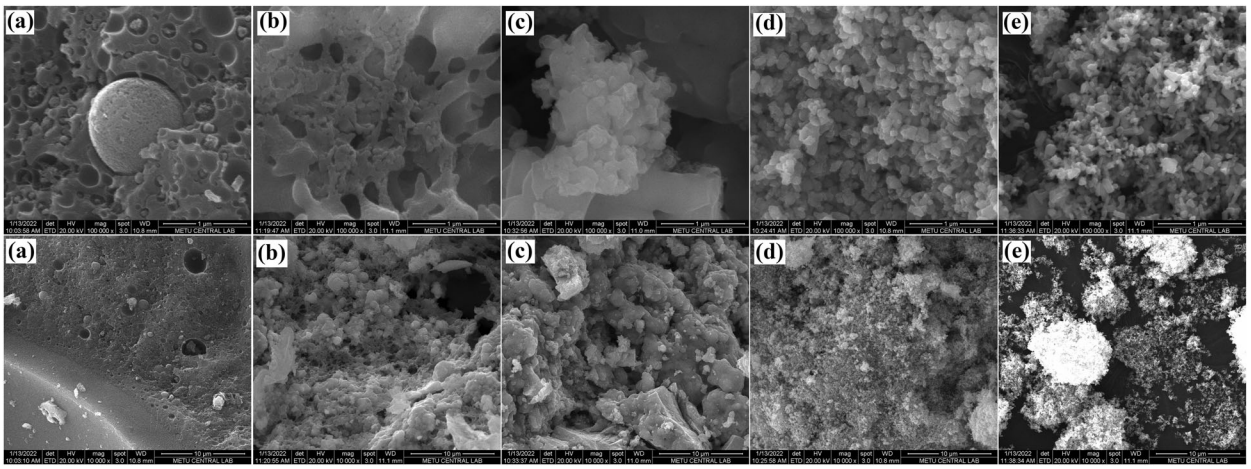

Fig. 2 SEM images of the **a** B_4C(100%)/ZnO, **b** B_4C(80%)/ZnO, **c** B_4C(67%)/ZnO, **d** B_4C(50%)/ZnO, and **e** B_4C(0%)/ZnO samples

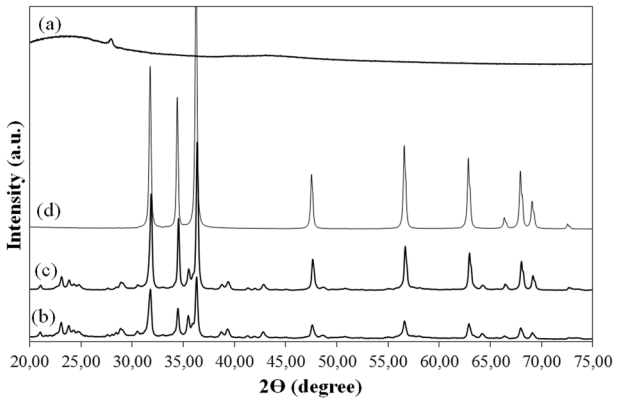

Fig. 3 XRD pattern of the **a** B_4C(100%)/ZnO, **b** B_4C(80%)/ZnO, **c** B_4C(50%)/ZnO, and **d** B_4C(0%)/ZnO samples

and B_4C nanoparticles on the SEM images (Fig. 2b–d). Figure 2e illustrates the ZnO nanoparticles in cylindrical shape. The cylindrical structures about 50 nm in diameter and 250 nm in length were imaged in an agglomerate structure.

3.3 XRD analysis

In order to evaluate the crystal structure of the B_4C (100%)/ZnO, B_4C(80%)/ZnO, B_4C(50%)/ZnO, and B_4C (0%)/ZnO samples, XRD patterns were examined as illustrated in Fig. 3. Figure 3a shows XRD pattern of pure B_4C obtained by the heat treatment of the polymer precursor, PVB, at 600 °C for 3 h. There is a broad diffraction peak between 20° and 30°, which was assigned to the amorphous carbon phase. It is understood that the formation of B_4C resulting from the carbothermal reduction reaction (2) of B_2O_3 is not fully completed at this relatively low temperature [18]. The broad diffraction peak was also attributed to the onset of crystallization of the amorphous carbon phase [28]. There is only one diffraction peak centered at 27.7°, which might belong to the rhombohedral crystal structure of B_4C [32]. Apart from the specified peak seen at 27.7°, the appearance of the peaks assigned to the rhombohedral B_4C crystal was not noticed. The complete conversion of the B_2O_3 phase and the amorphous carbon phase to the B_4C crystal was predicted to occur at higher temperatures.

$$2B_2O_3 + 7C \rightarrow B_4C + 6CO \quad (2)$$

On the XRD pattern of the B_4C(80%)/ZnO, B_4C(50%)/ZnO composites (Fig. 3b, c), there are diffraction peaks at 20.7°, 22.9, 23.7°, 28.5°, 35.4°, 39.1°, and 42.6°, and might be indexed to (101), (003), (012), (110), (104), (113), and (024) planes of the rhombohedral B_4C crystal (JCPDS file No. 26-232). The appearance of the diffraction peaks attributing to the rhombohedral B_4C crystal was noticed with the composites. In addition, no peak assigned to the amorphous carbon phase was observed on the XRD pattern of the composites, which means that B_4C was synthesized successfully from the carbothermal reduction of B_2O_3 in the presence of the ZnO nanocrystals. ZnO might act as a catalyst to lower the crystallization temperature of B_4C. When compared with the studies conducted on the synthesis of B_4C from the polymer precursor, B_4C crystals have been obtained relatively at lower heating temperatures in the presence of the ZnO nanoparticles [16, 18, 28]. As shown in Fig. 3d, the diffraction peaks observed at 31.7°, 34.4°, 36.1°, 47.5°, 56.6°, 62.8°, 66.3°, 67.9°, 69.0°, and 72.5°, belonging to (100), (002), (101), (102), (110), (103), (200), (112), (201), and (202) planes, can be attributed to the hexagonal wurtzite structure of ZnO (JCPDS card No. 89-7102). The characteristic diffraction peaks of ZnO can also be seen on the XRD spectrum of the composites at varying peak intensities.

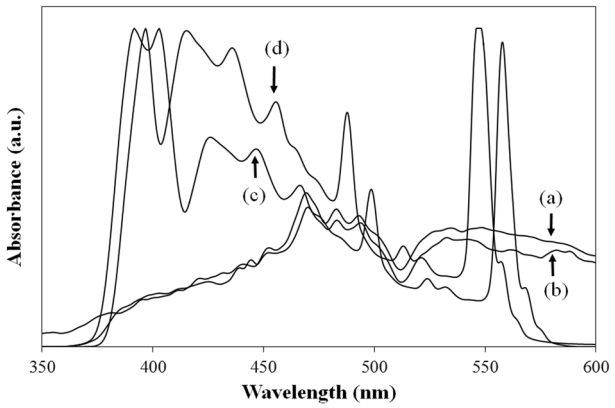

Fig. 4 The fluorescence spectrum of the **a** B_4C(100%)/ZnO, **b** B_4C(80%)/ZnO, **c** B_4C(50%)/ZnO, and **d** B_4C(0%)/ZnO samples

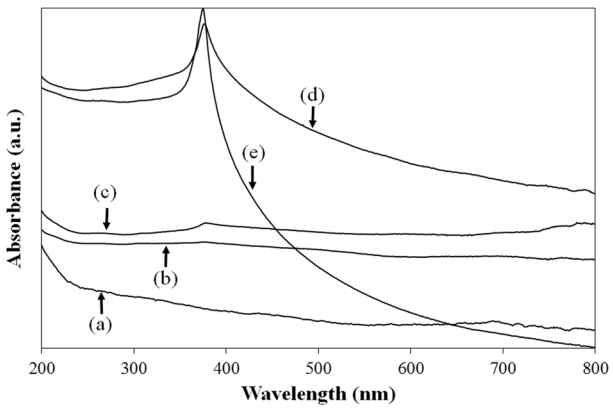

Fig. 5 UV–Vis absorption spectrum of **a** B_4C(100%)/ZnO, **b** B_4C(80%)/ZnO, **c** B_4C(67%)/ZnO, **d** B_4C(50%)/ZnO, and **e** B_4C(0%)/ZnO samples

3.4 Fluorescence study

The fluorescence study was conducted to investigate the photochemical property of the photocatalyst samples. The photocatalysts can generate electron–hole pairs after absorbing the light. Meanwhile, certain parts of the photo-induced charge carriers recombine by releasing energy in the form of fluorescence emission. Lower intensity of the fluorescence emission implies that the recombination rate of the photoexcited charge carriers is also low [27]. The fluorescence spectrum of pure B_4C and the B_4C(80%)/ZnO heterojunction composite exhibited emission peaks at around 470 nm and 540 nm (Fig. 4a, b), which might result from the recombination of the photoexcited electron–hole pair through the nonradiative relaxation process related to defects of B_4C [23]. The intensity of the emission centered both at 470 nm and 540 nm was slightly decreased with the heterojunction structure. On the fluorescence spectrum of pure ZnO, the emission peaks observed at around 414 nm and 546 nm were assigned to the Zn interstitial defects and the antisite defect of pure ZnO, respectively (Fig. 4d). The oxygen vacancy defect might be responsible for the emission peak observed at around 434 nm with pure ZnO. The reason for the specified emission peak might be the recombination of the photoexcited hole with the charge of the oxygen vacancy defect [33]. The B_4C(50%)/ZnO composite exhibited lower fluorescence emission peak at 434 nm, which supported the idea that combining B_4C with ZnO reduced the recombination rate of the photoexcited charge carriers on the photocatalysts. Due to the interaction of ZnO with B_4C in the composite structure, the fluorescence spectrum of pure ZnO exhibited a red shift.

3.5 UV–Vis absorption study

The UV–Vis absorption spectra of the as-prepared samples are illustrated in Fig. 5. The spectra indicated that pure ZnO nanoparticles mostly absorbed light in the UV region below 400 nm. When the ZnO nanoparticles were combined with the B_4C nanocrystals within the composite structure, the absorption band of ZnO enlarged to the visible region depending on the composition of B_4C. Hence, the B_4C/ZnO composites might be a suitable candidate as a photocatalyst under natural sunlight. The Tauc's relation (3) was used to estimate the optical band gap energy of the as-prepared photocatalyst samples [34]:

$$(\alpha hv)^2 = A\left(hv - E_g\right) \tag{3}$$

where α is the absorption coefficient, hv is the photon energy, A is a constant and E_g is the optical band gap, respectively. The optical band gap energy was estimated by extrapolating the linear part of the $(\alpha hv)^2$ vs. (hv) curve to the x-axis (Fig. 6). The optical band gap energy was found to be 1.70 eV, 1.85 eV, 1.95 eV, 2.85 eV, and 3.25 eV for B_4C(100%)/ZnO, B_4C(80%)/ZnO)B_4C, B_4C(67%)/ZnO, B_4C(50%)/ZnO)B_4C, and B_4C(0%)/ZnO, respectively. According to the results, combining ZnO with B_4C narrowed the optical band gap energy, exhibiting a red shift.

3.6 Photocatalytic performance

Figure S1 exhibits UV–Vis absorption spectra of methylene blue in the presence of as-prepared samples. The absorption intensity decreased gradually with time under the UVA light irradiation. The photocatalytic degradation efficiency of all samples was illustrated in Fig. 7. Pure ZnO (B_4C(0%)/ZnO) resulted in the highest photocatalytic activity. 99.2% of the model dye was degraded at 80 min. Among the composite samples, B_4C(50%)/ZnO exhibited the highest photocatalytic activity. The methylene blue degradation efficiency for B_4C(100%)/ZnO, B_4C(80%)/ZnO, B_4C(67%)/

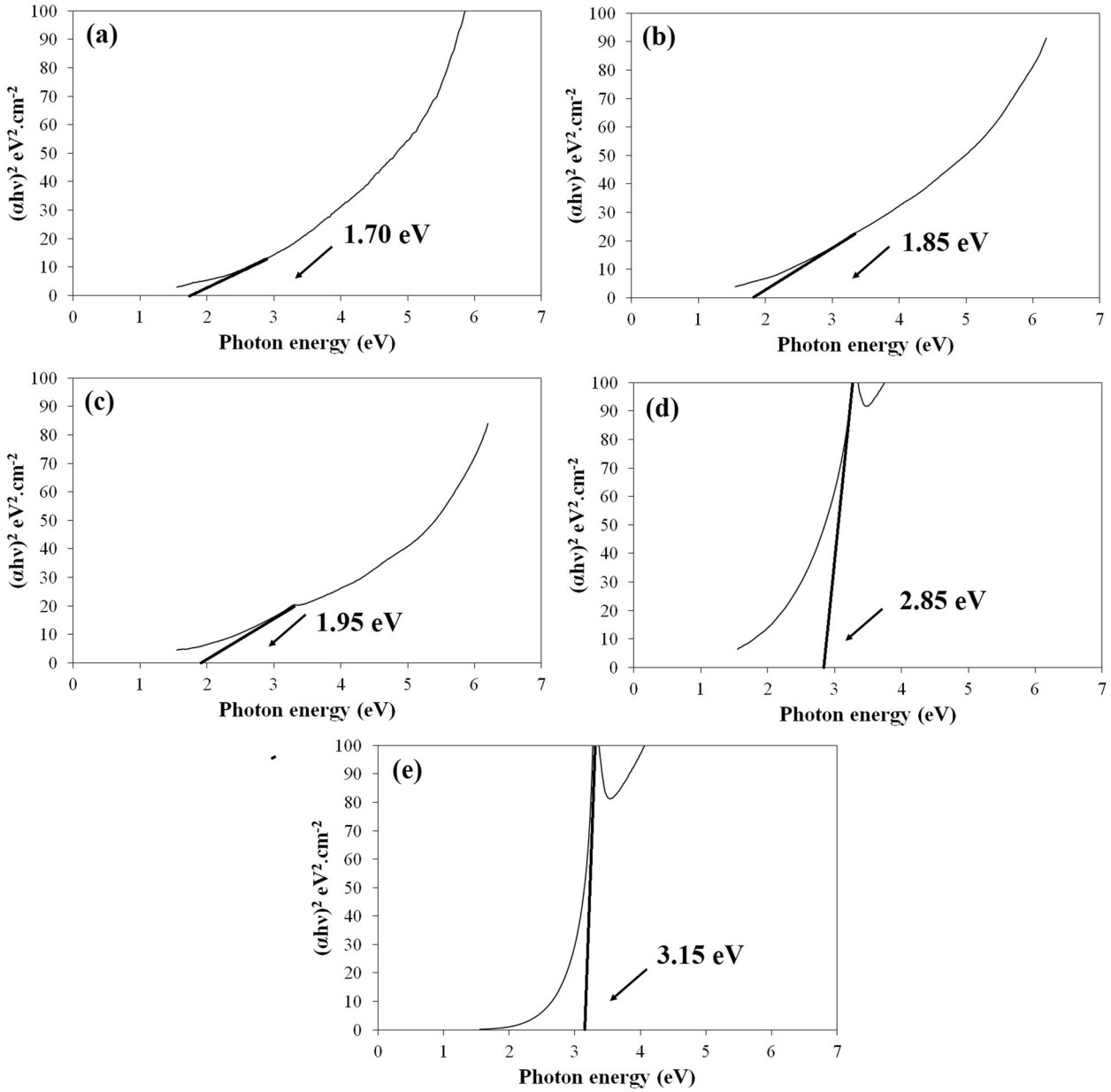

Fig. 6 Tauc's plot for the **a** B_4C(100%)/ZnO, **b** B_4C(80%)/ZnO, **c** B_4C(67%)/ZnO, **d** B_4C(50%)/ZnO, and **e** B_4C(0%)/ZnO samples

ZnO, and B_4C(50%)/ZnO is about 40.6%, 59.5%, 65.6%, and 73.9%, respectively, at 80 min. When compared with the literature, Rana et al. (2021) obtained 35.4% of photocatalytic norfloxacin degradation with pure B_4C under visible light at 90 min. [24] and Lv et al. (2021) obtained almost 20% of bisphenol S degradation with the BiOI/B_4C composite (50/50 wt/wt) under visible light at 30 min [25]. According to the literature data, it is clear that higher photocatalytic degradation efficiency was obtained with both pure B_4C and the composite structure (B_4C(50%)/ZnO). Figure 8 illustrates the proposed energy band structure and the photocatalytic degradation mechanism of the B_4C/ZnO heterojunction structure [35–38]. Due to the difference in work functions, combining B_4C and ZnO in the heterojunction structure could cause electrons to move from ZnO with low work function (5.2 eV) to B_4C with high work function (5.4 eV) until their Fermi levels align, leading to the formation of an electrostatic field at the interface of the heterojunction [37, 39]. The valence band and the conduction band of the photocatalysts might bend, which results to the formation a depletion layer around the heterojunction interface. When the heterojunction composite absorbs the UV light with photon energy equal or higher than the bandgap of the composite constituents, electrons

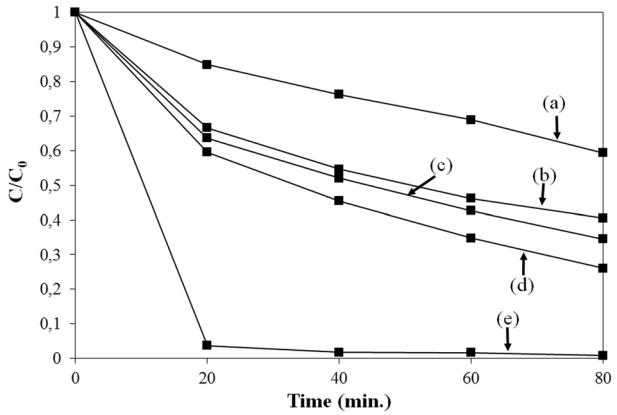

Fig. 7 The photocatalytic performance of the **a** B_4C(100%)/ZnO, **b** B_4C(80%)/ZnO, **c** B_4C(67%)/ZnO, **d** B_4C(50%)/ZnO, and **e** B_4C (0%)/ZnO samples under the UVA light irradiation

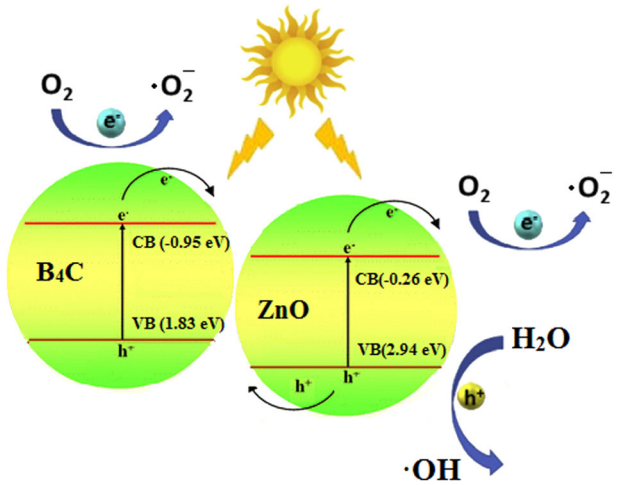

Fig. 8 The proposed photocatalytic degradation mechanism of the B_4C/ZnO heterojunction structure [37, 38]

can be excited from the valence band into the conduction band, giving rise to the formation of holes in the valence band. The electrostatic field around the depletion layer of the heterojunction structure might force the photoexcited electron–hole pairs to separate [37, 38].

The photoexcited electrons on the conduction band of B_4C could transfer to the conduction band of ZnO and the photogenerated holes on the valence band of ZnO could trasfer to the valence band of B_4C. Then, the photoexcited electron-hole pairs can participate in the photocatalytic degradation reactions. According to the redox potentials of the couple $O_2/\cdot O_2^-$, which is −0.33 eV vs. NHE, surface adsorbed O_2 molecules can be reduced by the photoinduced electrons of both B_4C and ZnO to superoxide anion radicals ($\cdot O_2^-$) [35]:

$$O_2 + e^- \rightarrow O_2^- \tag{4}$$

On the other hand, surface adsorbed H_2O molecules can be oxidized by the photoinduced holes of ZnO to hydroxyl radicals (·OH) since the valence band potential of ZnO is more positive than the redox couple $H_2O/\cdot OH$ for the formation of hydroxyl radicals (2.27 eV) according to the following equation [35]:

$$H_2O + h^+ \rightarrow OH + H^+ \tag{5}$$

The conduction band potential of both B_4C and ZnO is more negative than the redox potential (0.695 eV) for the formation of hydrogen peroxide (H_2O_2) from superoxide anion radicals. Hence, the superoxide radicals could react either with dissolved organic molecules or with hydrogen ions (H^+) to generate hydrogen peroxide radicals (H_2O_2), which can also trap the photoinduced electrons to generate additional hydroxyl radicals [36]:

$$O_2^- + 2H^+ + e^- \rightarrow H_2O_2 \tag{6}$$

$$H_2O_2 + e^- \rightarrow OH + OH^- \tag{7}$$

The hydroxyl radicals are strong oxidants, able to degrade organic molecules into harmless small molecules [36, 37]:

$$OH + \text{model dye} \rightarrow \text{degradation products} \tag{8}$$

On the basis of the proposed photocatalytic degradation mechanism (Fig. 8), it was concluded that the B_4C/ZnO heterojunction structure promotes the separation of the photoexcited charge carriers between the composite consitituents, reducing the recombination rate and improving the photocatalytic activity. When compared with pure B_4C (B_4C(100%)/ZnO), there was an enhancement in the photocatalytic activity of the B_4C (80%)/ZnO, B_4C(67%)/ZnO, and B_4C(50%)/ZnO composites (Fig. 7), supporting the idea that the charge separation was achieved successfully at the interface of the heterojunction structure.

The photocatalytic degradation of methylene blue in the presence of the as-prepared samples might fit the pseudo first-order reaction (9), given below [40]:

$$\ln(C_0/C) = kt \tag{9}$$

where C_0 is the concentration of the dye solution before the UV light irradiation, C is the concentration of the dye solution after the UV light irradiation and k is the degradation rate constant. The plot of $\ln(C/C_0)$ vs. irradiation time was used to determine the degradation rate constants (Fig. S2). The rate constant for B_4C(100%)/ZnO, B_4C(80%)/ZnO, B_4C(67%)/ZnO, B_4C(50%)/ZnO, and B_4C (0%)/ZnO was found to be 0.0065, 0.0126, 0.0143, 0.0178 and 0.0717 min^{-1}, respectively (Table 1). Compared to pure B_4C, a threefold increase in the reaction rate of the photocatalytic degradation was obtained with the B_4C (50%)/ZnO composite.

Table 1 The photocatalytic degradation rate of methylene blue in the presence of the as-prepared samples

Sample	k (min^{-1})	R^2
B_4C(100%)/ZnO	0.0065	0.9900
B_4C(80%)/ZnO	0.0126	0.9096
B_4C(67%)/ZnO	0.0143	0.9393
B_4C(50%)/ZnO	0.0178	0.9639
B_4C(0%)/ZnO	0.0717	0.6092

3.7 Reusability study

After the first cycle of the degradation experiment, the B_4C(50%)/ZnO composite nanoparticles were separated from the dye solution and then dried. The dried B_4C(50%)/ZnO nanoparticles were used for the subsequent photocatalytic degradation cycles. According to Fig. 9, a consistent reduction was observed in the photocatalytic degradation efficiency of the B_4C(50%)/ZnO composite for the subsequent cycle tests. 47.9% of the model dye was degraded at 80 min. after four-cycle runs. The photocatalyst nanoparticles were isolated from the dye solution and dried. They were used in the next photocatalytic degradation reaction without applying any chemical or physical treatments. The aim was to determine how long the photocatalyst could maintain its effectiveness without any cleaning. After four cycles, approximately 26% loss in the photocatalytic degradation efficiency was observed. The active surface area of the photocatalyst nanoparticles might reduce as a result of the adsorbed methylene blue molecules, blocking the active surface area, and thus the photocatalytic degradation efficiency might reduce. On the other hand, this decrease in the photocatalytic degradation efficiency could be assigned to the photocorrosion in the recycle tests. The photoinduced holes might result in the photoinduced dissolution of Zn^{2+} ions on the ZnO crystals, which greatly affect the photocatalytic activity [41].

3.8 Effect of scavengers on the photocatalytic performance

The effect of different scavengers was studied to reveal the photocatalytic degradation mechanism of the B_4C(50%)/ZnO composite. The photoexcited electron-hole pairs, superoxide, and hydroxyl radicals are the probable active species involved in the photocatalytic degradation of organic molecules. To determine the contribution of the specified active species to the photocatalytic degradation, electron, hole, and radical scavengers were added separately to the reaction medium. According to Fig. 9, the addition of the electron scavenger slightly increased the photocatalytic degradation efficiency from 73.9% to 76.6% and the addition of the hole scavenger slightly reduced the degradation efficiency from 73.9% to 70.4%. These results revealed that the photoexcited holes were slightly more active compared to the photoexcited electrons in the photocatalytic degradation reactions. The photocatalytic degradation efficiency reduced considerably when the superoxide radical scavenger and the hydroxyl radical scavenger were added separately to the reaction medium. Methylene blue was degraded 16.1% and 22.2% within 80 min by the B_4C(50%)/ZnO composite in the presence of the superoxide radical scavenger and the hydroxyl radical scavenger, respectively (Fig. 9). Based on the scavengers' test, it is clear that both the hydroxyl and superoxide radicals contributed significantly to the photocatalytic degradation reaction of methylene blue.

3.9 Effect of pH on the photocatalytic performance

The degradation of the dye molecules takes place on the surface of photocatalyst and the adsorption of the dye molecules on the photocatalyst is an important step in the photocatalytic degradation reaction. It is a known fact that the dye molecules, exhibiting high adsorption rate, can degrade faster. Since methylene blue is a positively charged organic dye, it can be adsorbed on the surfaces of the photocatalyst if the pH of the solution is above the photocatalyst's point of zero charge [42, 43]. According to Fig. 10, higher pH value (pH = 10) could make the surface of the B_4C(50%)/ZnO composite become negatively charged and promote the electrostatic attraction between the photocatalyst and the dye molecules, enhancing the photocatalytic degradation efficiency. 97.1% of methylene blue was degraded after 80 min. of UVA irradiation at pH = 10. In addition, if the pH value of the solution is above 7, there can be more hydroxide ions, reacting with the photoexcited holes to generate additional hydroxyl radicals [42]. Since the valence band potential of ZnO is more positive than the redox potential of the couple $H_2O/\cdot OH$, which is 2.73 eV at pH = ~11, surface adsorbed water molecules can be reduced at the surface of ZnO when the pH value is above 7 [44]. The combined effect of increased adsorption affinity of the dye molecules to the photocatalyst surface and additional hydroxyl radicals might be the reason for the increase in the photocatalytic degradation efficiency.

On the other hand, lower pH value (pH = 3) could make the surface of the photocatalyst become positively charged and inhibit the electrostatic attraction between the B_4C(50%)/ZnO nanoparticles and the dye molecules, which might reduce the photocatalytic degradation efficiency. Methylene blue was degraded 63.1% after 80 min. of UVA irradiation at pH = 3. According to the literature, the redox potential of the couple $H_2O/\cdot OH$ for the formation of hydroxyl radicals, which is 1.23 eV at pH = ~1, is more

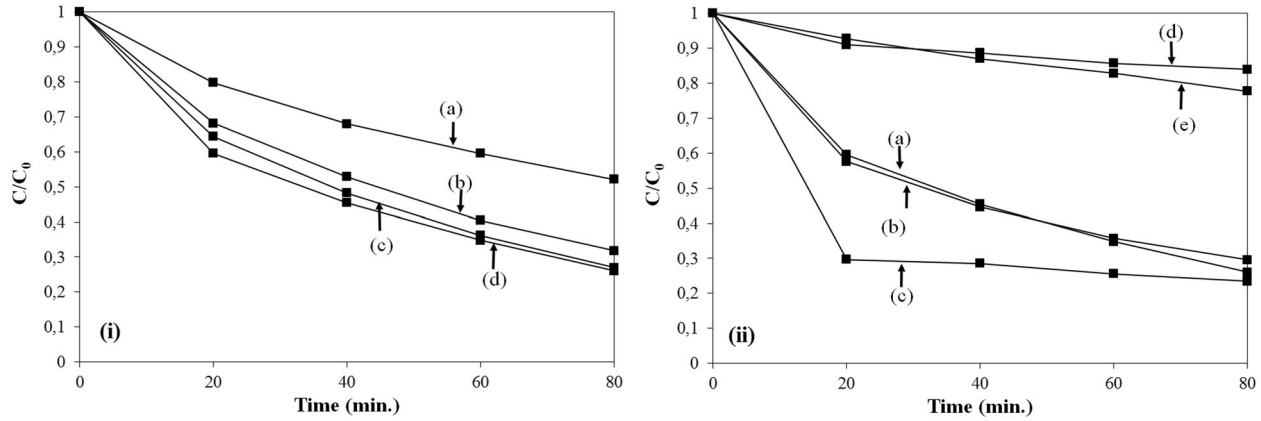

Fig. 9 (i) The reusability results of the methylene blue degradation experiment in the presence of the B_4C(50%)/ZnO composite; (ii) The photocatalytic performance of **a** B_4C(50%)/ZnO composite without a scavenger, **b** B_4C(50%)/ZnO composite with the hole scavenger, **c** B_4C(50%)/ZnO composite with the electron scavenger, **d** B_4C(50%)/ZnO composite with the superoxide radical scavenger, and **e** B_4C(50%)/ZnO composite with the hydroxyl radical scavenger under the UVA light irradiation

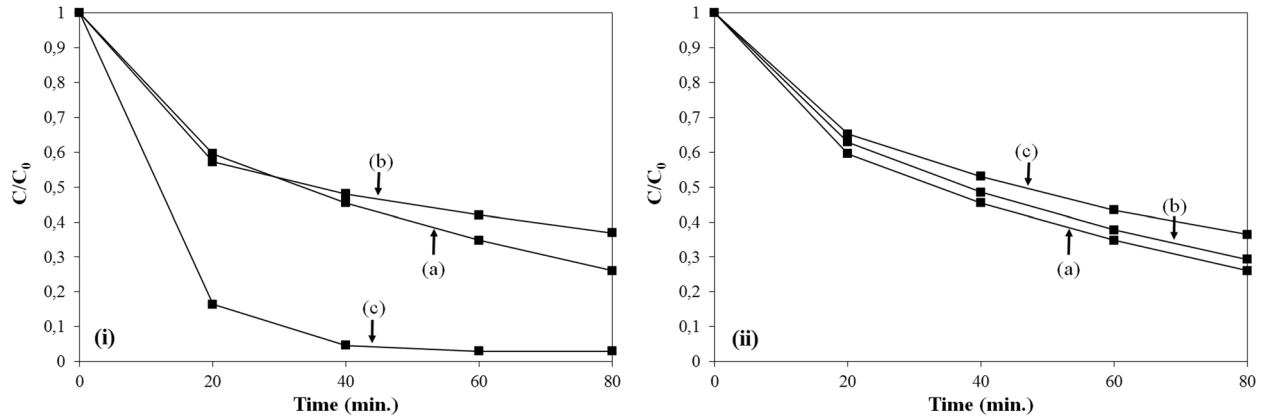

Fig. 10 (i) The photocatalytic degradation efficiency of the B_4C(50%)/ZnO composite at the pH of **a** 6.7 (natural pH), **b** 3 and **c** 10 under the UVA light irradiation; (ii) The photocatalytic degradation efficiency of the B_4C(50%)/ZnO composite at **a** 22 °C, **b** 42 °C, and **c** 62 °C under the UVA light irradiation

negative than the valence band potential of both ZnO and B_4C [44]. In terms of reaction thermodynamics, there is no hindrance to the formation of radicals on the catalyst surface in an acidic medium.

3.10 Effect of temperature on the photocatalytic performance

If the reaction temperature of the photocatalytic degradation increases, the mobility of the charge carriers decreases and the number of charge carriers increases, which can dominate the mobility reduction. That is, more photoinduced electron–hole pairs can reach to the photocatalyst surface, at which they reduce and oxidize surface adsorbed O_2 and H_2O molecules, respectively. Hence, the temperature rise can improve photocatalytic efficiency [45]. On the other hand, the photoexcited charge carriers can recombine faster at high temperatures. According to the literature, an increase in the reaction temperature caused an increase in the recombination rate of the photoexcited charge cariers and a decrease in the photocatalytic activity [46]. The dye molecules must be adsorbed to the surface before they are degraded by the photocatalyst. It is a known fact that the adsorption reaction is an exothermic process and the desorption reaction is an endothermic process. That is, the temperature rise favors the desorption of the dye molecules from the photocatalyst surface [45]. When the reaction temperature increases to 42 °C and 62 °C, the dye molecules might desorb faster from the surface of the B_4C(50%)/ZnO composite. After 80 min. of UVA irradiation, the photocatalytic degradation efficiency of the B_4C(50%)/ZnO composite reduced to 70.7% and 63.6% at 42 °C and 62 °C, respectively (Fig. 10). According to the above discussion, the temperature rise might dominate the recombination of the charge carriers and suppress the adsorption of the dye molecules on the photocatalyst surface.

4 Conclusion

B_4C/ZnO composite photocatalysts were prepared through the heat treatment of the polymer precursor, polyvinyl borate composite, synthesized through the condensation reaction of polyvinyl alcohol and boric acid in the presence of the ZnO nanoparticles. The photocatalytic degradation efficiency of the composites was higher than that of pure B_4C under the UV light irradiation. The B_4C(50%)/ZnO composite exhibited the highest photocatalytic degradation efficiency among the composite samples, prepared. According to the reusability experiments, after four cycles of the photocatalytic degradation tests, ~26% loss in the photocatalytic degradation efficiency was observed. Scavenger experiments revealed that the photoinduced holes, the superoxide radicals, and the hydroxyl radicals actively participated in the photocatalytic degradation of methylene blue. SEM images illustrated the stable interaction between the composite constituents. FTIR analysis exhibited the B-C bonds of B_4C and XRD pattern exhibited the characteristic diffraction peaks of B_4C, proving that B_4C and B_4C/ZnO composites were synthesized successfully. B_4C and ZnO might have formed a heterojunction structure to suppress the recombination rate of the photoinduced charge carriers. The reduction in the recombination rate of the composites was determined by the reduction in the fluorescence emission peaks of the composites.

Author contributions All authors contributed to the study's conception and design. Material preparation, data collection, and analysis were performed by OK and HNK.

Compliance with ethical standards

Conflict of interest The authors have no relevant financial or non-financial interests to disclose. The authors declare no competing interests.

Publisher's note Springer Nature remains neutral with regard to jurisdictional claims in published maps and institutional affiliations.

References

1. Ma MD, Yang RL, Zhang C, Wang BC, Zhao ZS, Hu WT, Liu ZY, Yu DL, Wen FS, He JL (2019) Direct large-scale fabrication of C-encapsulated B4C nanoparticles with tunable dielectric properties as excellent microwave absorbers. Carbon 148:504–511
2. Hajizamani M, Alizadeh A, Ehsani N (2012) Deposition of a Ni3P nano-scale layer on B4C nanoparticles by simple electroless plating in an acidic bath. Appl Nanosci 2:417–421
3. Ma MD, Li PH, Li BZ, Wu YJ, Gao YF, Hu WT, Gao GY, Zhao ZS, Yu DL, He JL (2019) One-step synthetic route and sintering for carbon-coated B4C nanoparticles. J Alloy Compd 782:263–269
4. Sharifi EM, Karimzadeh F, Enayati MH (2011) Mechanochemical assisted synthesis of B4C nanoparticles. Mater Sci Forum 22:354–358
5. Singh P, Singh B, Kumar M, Kumar A (2014) One step reduction of boric acid to boron carbide nanoparticles. Ceram Int 40:15331–15334
6. Lee JH, Won CW, Joo SM, Maeng DY (2000) Preparation of B4C powder from B2O3 oxide by SHS process. J Mater Sci Lett 19:951–954
7. Jazirehpour M, Alizadeh A (2009) Synthesis of boron carbide core-shell nanorods and a qualitative model to explain formation of rough shell nanorods. J Phys Chem C113:1657–1661
8. Jung CH, Lee MJ, Kim CJ (2004) Preparation of carbon-free B4C powder from B2O3 oxide by carbothermal reduction process. Mater Lett 58:609–614
9. Ishikawa Y, Sasaki T, Koshizaki N (2010) Submicron-sized boron carbide particles encapsulated in turbostratic graphite prepared by laser fragmentation in liquid medium. J Nanosci Nanotechnol 10:5467–5470
10. Chang B, Gersten BL, Szewczyk ST, Adams JW (2007) Characterization of boron carbide nanoparticles prepared by a solid state thermal reaction. Appl Phys A 86:83–87
11. Wang SJ, Li YF, Xing XL, Jing XL (2018) Low-temperature synthesis of high-purity boron carbide via an aromatic polymer precursor. J Mater Res 33:1659–1670
12. Li J, Cao K, Li J, Liu MF, Zhang S, Yang JX, Zhang ZW, Li B (2018) Synthesis and ceramic conversion of a new organodecaborane preceramic polymer with high-ceramic-yield. Molecules 23:2461
13. Kesici AD, Kiraz N (2021) Low-temperature synthesis of boron carbide nanofibers via electrospinning to reinforce composites. Chem Pap 75:5839–5848
14. Hanniet Q, Boussmen M, Barés J, Huon V, Hanniet Quentin, Boussmen Moustapha, Barés Jonathan, Huon Vincent, Igor Iatsunskyi I, Coy E, Bechelany M, Gervais C, Voiry D, Miele P, Salameh C (2020) Investigation of polymer-derived Si–(B)–C–N ceramic/reduced graphene oxide composite systems as active catalysts towards the hydrogen evolution reaction. Sci Rep 10:22003
15. Volger KW, Kroke E, Gervais C, Saito T, Babonneau F, Riedel R, Iwamoto Y, Hirayama T (2003) B/C/N materials and B4C synthesized by a non-oxide sol-gel process. Chem Mater 15:755–764
16. Kakiage M, Tahara N, Yanagidani S, Yanase I, Kobayashi H (2011) Effect of boron oxide/carbon arrangement of precursor derived from condensed polymer-boric acid product on low-temperature synthesis of boron carbide powder. J Ceram Soc Jpn 119:422–425
17. Shawgi N, Li SX, Wang S (2017) A Novel method of synthesis of high purity nano plated boron carbide powder by a solid-state reaction of poly (vinyl alcohol) and boric acid. Ceram Int 43:10554–10558
18. Yanase I, Ogaware R, Kobayashi H (2009) Synthesis of boron carbide powder from polyvinyl borate precursor. Mater Lett 63:91–93
19. Mondal S, Banthia AK (2005) Low-temperature synthetic route for boron carbide. J Eur Ceram Soc 25:287–291
20. Liu JK, Wen SH, Hou Y, Zuo F, Beran GJO, Feng PY (2013) Boron carbides as efficient, metal-free, visible-light-responsive photocatalysts. Angew Chem Int Ed 52:3241–3245
21. Yan DJ, Liu JK, Fu XC, Liu PL, Luo HA (2019) Low-temperature synthesis of mesoporous boron carbides as metal-free photocatalysts for enhanced CO2 reduction and generation of hydroxyl radicals. J Mater Sci 54:6151–6163
22. Zhang XJ, Wang L, Du QC, Wang ZY, Ma SG, Yu M (2016) Photocatalytic CO_2 reduction over B4C/C3N4 with internal electric field under visible light irradiation. J Colloid Interface Sci 464:89–95
23. Zhang XJ, Yang JP, Cai TC, Zuo GQ, Tang CQ (2018) TiO2 nanosheets decorated with B4C nanoparticles as photocatalysts for solar fuel production under visible light irradiation. Appl Surf Sci 443:558–566

24. Rana A, Kumar A, Sharma G, Naushad M, Bathula C, Stadler FJ (2021) Pharmaceutical pollutant as sacrificial agent for sustainable synergistic water treatment and hydrogen production via novel Z-scheme Bi7O9I3/B4C heterojunction photocatalysts. J Mol Liq 343:117652
25. Lv YF, Liu Y, Wei J, Li MY, Xu DY, Lai B (2021) Bisphenol S degradation by visible light assisted peroxymonosulfate process based on BiOI/B4C photocatalysts with Z-scheme heterojunction. Chem Eng J 417:129188
26. Yu WW, Cao SY, Wang C, Chen CS (2016) Constructing MnO2/single crystalline ZnO nanorod hybrids with enhanced photocatalytic and antibacterial activity. J Solid State Chem 239:131–138
27. Chen SF, Zhao W, Liu W, Zhang SJ (2009) Preparation, characterization and activity evaluation of p-n junction photocatalyst p-NiO/n-ZnO. J Sol-Gel Sci Technol 50:387–396
28. Barros PM, Yoshida OVP, Schiavon MA (2006) Boron-containing poly(vinyl alcohol) as a ceramic precursor. J Non-Cryst Solids 352:3444–3450
29. Wang DS, Wang YH, Li XY, Luo QZ, An J, Yue HX (2008) Sunlight photocatalytic activity of polypyrrole-TiO_2 nanocomposites prepared by 'in situ' method. Catal Commun 9:1162–1166
30. Aksoy S, Caglar Y (2019) Synthesis of Mn-doped ZnO nanopowders by MW-HTS and its structural, morphological and optical characteristics. J Alloy Compd 781:929–935
31. Ebrahimi-Kahrizsangi R, Torabi O (2012) Combination of mechanochemical activation and self-propagating behavior for the synthesis of nanocomposite Al_2O_3/B4C powder. J Alloy Compd 514:54–59
32. SarithaDevi HV, Swapna MS, Ambadas G, Sankararaman S (2018) Low-temperature green synthesis of boron carbide using aloe vera. Chin Phys B 27:107702
33. Estrada-Urbina J, Cruz-Alonso A, Santander-González M, Méndez-Albores M, Vázquez-Durán A (2018) Nanoscale zinc oxide particles for improving thephysiological and sanitary quality of a Mexican Landrace of red maize. Nanomaterials 8:247
34. Qiu YF, Fan HB, Tan GP, Yang ML, Yang XX, Yang SH (2014) Effect of nitrogen doping on the photo-catalytic properties of nitrogen doped ZnO tetrapods. Mater Lett 131:64–66
35. Villa K, Galan-Mascaros JR (2021) Nanostructured photocatalysts for the production of methanol from methane and water. Chemsuschem 14:2023–2033
36. Gao HJ, Yang H, Wang SF (2018) Hydrothermal synthesis, growth mechanism, optical properties and photocatalytic activity of cubic SrTiO3 particles for the degradation of cationic and anionic dyes. Optik 175:237–249
37. Zheng LR, Zheng YH, Chen CQ, Zhan YY, Lin XY, Zheng Q, Wei KM, Zhu JF (2009) Network structured SnO2/ZnO heterojunction nanocatalyst with high photocatalytic activity. Inorg Chem 48:1819–1825
38. Lu C, Zhimin BZ, Qin C, Dai L, Zhu A (2016) Facile fabrication of heterostructured cubic-CuFe2O4/ZnO nanofibers (c-CFZs) with enhanced visible-light photocatalytic activity and magnetic separation. RSC Adv 6:110155–110163
39. He CS, Li ZB, Wang WL (2012) Work function of boron carbide: a DFT calculation. Surf Rew Lett 19:1250040
40. Wan Q, Wang TH, Zhao JC (2005) Enhanced photocatalytic activity of ZnO nanotetrapods. Appl Phys Lett 87:083105
41. Yang J, Zeng XY, Yang WL, Gao MZ (2015) Effect of exposure time on the growth of self-supporting ZnO nanowire arrays and their photocatalytic behavior. Mater Sci Eng B-Adv Funct Solid-State Mater 191:28–32
42. Kazeminezhad I, Sadollahkhani A (2016) Influence of pH on the photocatalytic activity of ZnO nanoparticles. J Mater Sci Mater Electron 27:4206–4215
43. Cheng Q, Wang C, Doudrick K, Chan CK (2015) Hexavalent chromium removal using metal oxide photocatalysts. Appl Catal B-Environ 176:740–748
44. Kwon BG, Yoon J (2009) Superoxide anion radical: principle and application. J Korean Ind Eng Chem 20:593–602
45. Chen YW, Hsu YH (2021) Effects of reaction temperature on the photocatalytic activity of TiO_2 with Pd and Cu cocatalysts. Catalysts 11:966
46. Kumar A, Pandey GA (2017) Review on the factors affecting the photocatalytic degradation of hazardous materials. Mater Sci Eng Int J 1:106–114